2-1-2011

Remote observations of ion temperatures in the quiet time magnetosphere

A. M. Keesee

N. Buzulukova

J. Goldstein

D. J. McComas

E. E. Scime

See next page for additional authors

Recommended Citation

Keesee, A. M., N. Buzulukova, J. Goldstein, D. J. McComas, E. E. Scime, H. Spence, M.-C. Fok, andK. Tallaksen (2011), Remote observations of ion temperatures in the quiet time magnetosphere,Geophys. Res. Lett., 38, L03104, doi:10.1029/2010GL045987.

Remote observations of ion temperatures in the quiet time magnetosphere

A. M. Keesee,[1] N. Buzulukova,[2] J. Goldstein,[3,4] D. J. McComas,[3,4] E. E. Scime,[1] H. Spence,[5] M.-C. Fok,[2] and K. Tallaksen[1]

Received 26 October 2010; revised 21 December 2010; accepted 30 December 2010; published 5 February 2011.

[1] Ion temperature analysis of the first energetic neutral atom images of the quiet-time, extended magnetosphere provides evidence of multiple regions of ion heating. This study confirms the existence of a dawn-dusk asymmetry in ion temperature predicted for quiescent magnetospheric conditions by Spence and Kivelson (1993) and demonstrates that it is an inherent magnetospheric feature. **Citation:** Keesee, A. M., N. Buzulukova, J. Goldstein, D. J. McComas, E. E. Scime, H. Spence, M.-C. Fok, and K. Tallaksen (2011), Remote observations of ion temperatures in the quiet time magnetosphere, *Geophys. Res. Lett.*, *38*, L03104, doi:10.1029/2010GL045987.

1. Introduction

[2] Measurements of ion temperatures throughout the magnetosphere provide an important description of magnetospheric dynamics during both geomagnetically active and quiet times. Global ion temperature maps using *in situ* measurements have been created in previous studies, but required accumulation of years of data [*Wang et al.*, 2006; *Guild et al.*, 2008; *Denton and Taylor*, 2008] or were inferred using ionospheric plasma measurements by the DMSP spacecraft [*Wing and Newell*, 2002]. Energetic neutral atom (ENA) flux imaging provides measurements of the magnetospheric ion populations (which become ENAs through charge exchange collisions) over short timescales and with a global view of the magnetosphere. The TWINS spacecraft [*McComas et al.*, 2009] take advantage of multiple viewing locations to obtain high-spatial resolution maps of the ENA flux emitted from the entire magnetosphere. In nearly all previous ENA studies of the terrestrial magnetosphere, the intervals studied were dominated by geomagnetically active periods because it is during those times that the ENA fluxes are the largest. Only one study, using data from the IMAGE spacecraft, reported ENA images of the quiet-time magnetosphere [*Zaniewski et al.*, 2006].

[3] In this paper, we present the first ENA images of the quiet-time (Dst index > −30 nT) magnetosphere obtained by the TWINS spacecraft. We find that the spatial distribution of parent ion distribution temperatures is consistent with predictions of a model that accounts for both the duskward gradient/curvature drift and the earthward E × B drift of ions in a two-dimensional magnetic geometry [*Spence and Kivelson*, 1993]. Thus, during intervals without significant geomagnetic activity, there is a significant net duskward displacement of the pressure-bearing ions. To build up sufficient statistics for imaging, 138.7 hours of ENA data (a little less than six days of remote observations during January and February of 2009) from both TWINS spacecraft are combined into a single image in Geocentric Solar Magnetospheric (GSM) coordinates. GSM coordinates are employed so that ENA fluxes obtained during different orbits and from different vantage points are mapped to a single, common image plane.

2. Observations and Mapping Methodology

[4] Since the details of the TWINS instrument [*McComas et al.*, 2009] and the remote ion temperature determination procedure have been described in detail elsewhere [*Scime et al.*, 2002; *Zaniewski et al.*, 2006; *Keesee et al.*, 2008], only a brief outline of the instrumentation and the analysis method is provided here. The TWINS ENA instrument is a time-of-flight (TOF) resolving, imaging ENA camera. Full TOF and angle information were available for each ENA count used in this study. A detailed model of the instrument response is used to accurately sort the data into actuation angle, polar angle and TOF bins.

[5] To accommodate the varying vantage-point of the satellite's orbital motion, the measured ENA fluxes are mapped to the *xy*-plane (GSM coordinates) that is divided into 0.5 × 0.5 R_E bins. For each pixel in an ENA image, the intersection of the associated field-of-view (FOV) with the GSM *xy*-plane is calculated. The ENA flux divided by the square of the LOS, ENA emissivity, for that pixel is divided among the *xy*-plane bins in amounts proportional to the fractional area of the FOV that intersects each bin. This algorithm is used because the fixed angular resolution of the instrument yields a FOV that increases as a function of distance from the Earth. If the intersection location falls outside of a modeled magnetosphere boundary [*Shue et al.*, 1997], the flux is ignored. Approximately 12% of the mapped pixels are excluded based on this constraint. An average flux for each bin is calculated by dividing the total flux by the number of times an instrument FOV pixel overlapped a particular spatial bin. To ensure good viewing geometry, ENA data is included only when the TWINS satellites are at least 4 R_E above the *xy*-plane. The ENA fluxes are converted to LOS-integrated, density-weighted phase space densities (psd), $j_{ENA}/\sigma E$, using the known energy dependent charge-exchange cross section, σ. The ion temperatures are calcu-

[1]Department of Physics, West Virginia University, Morgantown, West Virginia, USA.
[2]NASA Goddard Space Flight Center, Greenbelt, Maryland, USA.
[3]Southwest Research Institute, San Antonio, Texas, USA.
[4]Department of Physics and Astronomy, University of Texas at San Antonio, San Antonio, Texas, USA.
[5]Institute for the Study of Earth, Oceans, and Space, University of New Hampshire, Durham, New Hampshire, USA.

0094-8276/11/2010GL045987

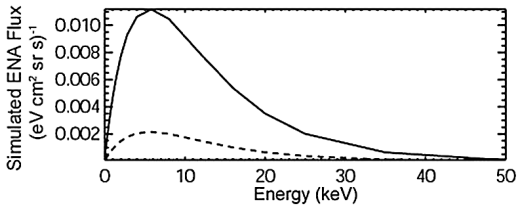

Figure 1. Simulated ENA flux intensity (solid line) using CRCM for a pixel that would map to $x = -9\ R_E$ for a satellite position of $(x, y, z) = (0,0,5\ R_E)$. The dashed line indicates the contribution to the ENA flux intensity from within 6 R_E of the satellite.

lated from the psd spectra, assuming a Maxwellian parent ion distribution [*Scime et al.*, 2002].

[6] *McComas et al.* [2002] showed that ENA fluxes were regularly observed by the IMAGE spacecraft from at least 20 R_E downtail during quiet conditions, and further downtail as the plasma sheet density increased. To determine if the line-of-sight (LOS) ENA measurements are likely to be dominated by emission from nearby the spacecraft and not distant regions where the FOV maps to the equatorial plane, we used the Comprehensive Ring Current Model (CRCM) [*Fok et al.*, 2001] to calculate the flux of ENAs as a function of energy along a typical LOS. Figure 1 shows the calculated ENA flux (for protons) versus energy for a LOS that intersects the *xy*-plane at $(x, y, z) = (-9\ R_E,0,0)$ for a theoretical satellite position of $(0,0,5\ R_E)$ from a CRCM simulation with static B-field for 22 July 2009 around 17 UT during relatively quiet conditions [*Fok et al.*, 2010] and for a spherically symmetric geocorona. The solid line shows the total calculated ENA flux while the dashed line indicates the contribution from ENAs originating within a sphere of radius 6 R_E of the Earth. It can be seen that the majority of ENA flux originates from outside 6 R_E. Thus, even though the neutral hydrogen density in the foreground of the instrument view is higher than that in the plasma sheet, the ENA flux is dominated by flux from the distant plasma sheet regions in the FOV. Because the flux is dominated by the hottest location along the LOS [*Hutchinson*, 1987] and the ion temperature decreases as a function of distance downtail [*Tsyganenko and Mukai*, 2003], the flux is assigned where the LOS intersects the *xy*-plane rather than where the L-value with closest approach intersects. While the inner magnetosphere is somewhat more complex, it has been shown previously that hot features such as the ring current dominate the temperature maps [*Zaniewski et al.*, 2006]. To reduce the effects of energetic particle background and counting noise in the highest energy bins, a background level has been subtracted from the ENA flux. The ENA fluxes that appear within 5° of the Earth's limb in instrument coordinates and that are mapped to within three R_E of the Earth are excluded as our analysis methodology fails for this optically thick region. The minimum satellite height of 4 R_E reduces the FOVs that pass through this region but map outside of it. As shown previously [*Zaniewski et al.*, 2006], oxygen neutrals grouped together with hydrogen neutrals by these types of ENA instruments typically fall into the lowest energy bin and have little to no effect on the ion temperature determination.

[7] In previous studies using similar energy range ENA data from the MENA instrument aboard the IMAGE spacecraft, the assumption that ion temperatures in the equatorial plane dominate the remotely obtained ENA fluxes (our ENA analysis methodology) was validated by comparison to *in situ* ion temperature measurements from multiple magnetospheric

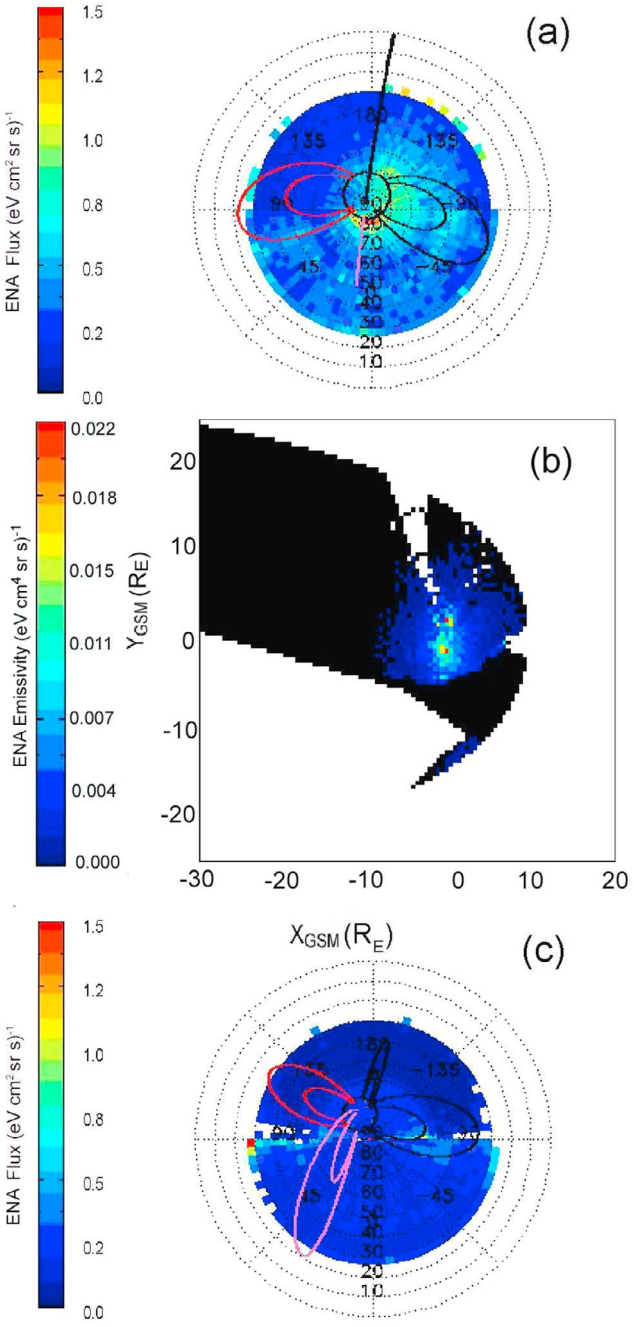

Figure 2. (a) TWINS-1 image of 9 keV neutrals, integrated over 27.5 minutes, during a weak geomagnetic storm that occurred on June 15, 2008. Dipole magnetic field lines are drawn at L = 4 and L = 8, with those at 1200 h MLT (noon) in red and those at 1800 h MLT in light purple, while midnight and dawn are in black. The Earth's limb and terminator are delimited. (b) The ENA emissivity calculated from the data in Figure 2a mapped onto the GSM *xy* plane. The Sun is to the right. (c) TWINS-1 image of 9 keV neutrals, integrated over 27.5 minutes, during a quiet magnetospheric interval on January 2, 2009.

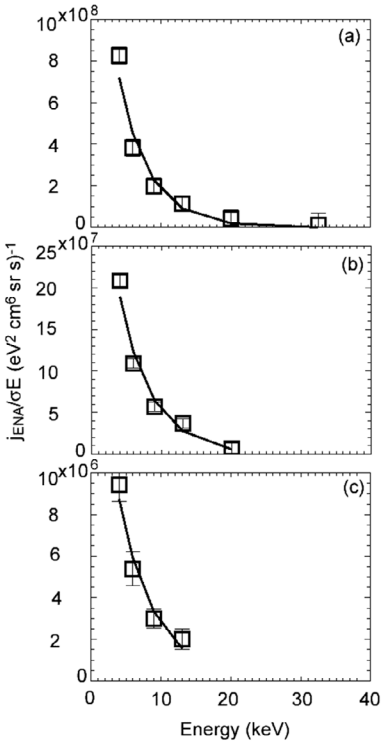

Figure 3. LOS-integrated, density-weighted phase space density (squares) versus energy and Maxwellian fit (line) for the bins containing (x, y) (a) (−5,−2), (b) (−12, 5), and (c) (−27, 9), yielding temperatures of 4.4 keV, 4.6 keV, and 5.2 keV, respectively.

spacecraft. The ENA-derived ion temperatures at the location of the equatorial projection were found to be in excellent agreement with ion temperatures from four magnetospheric plasma analyzer (MPA) instruments [*Bame et al.*, 1993] in geosynchronous orbit (6.6 R_E) and from Geotail [*Frank et al.*, 1994] at $x = -9$ R_E [*Keesee et al.*, 2008]. More sophisticated ion temperature determination methods, i.e., full inversions of measured high-energy ENA fluxes, yielded nearly identical inner magnetosphere ion temperatures in the equatorial plane [*Zhang et al.*, 2005].

[8] A typical TWINS image during a moderately geomagnetically active interval (Dst = −38 nT; 15 June 2008, 5:31–5:58 UT) for 9 keV ENAs from TWINS-1 is shown in Figure 2a in TWINS viewing coordinates for an integration time of 27.5 minutes, equivalent to 20 cycles of the instrument actuator. The ENA emissivity mapped onto the GSM xy-plane for that interval is shown in Figure 2b. Spatial bins with zero flux are white and the bins that appear black have non-zero flux values that are small due to the fractional mapping algorithm. A typical quiet-time TWINS ENA image from TWINS-1 (2 Jan 2009, 7:59–8:27 UT), also integrated over 27.5 minutes, for the same energy is shown in Figure 2c. Note that for the same integration interval, considerably less structure is evident in the quiet-time image than in the image obtained during the geomagnetically active interval. The horizontal band of slightly increased count rates adjacent to the band of missing data is sunlight contamination in the instrument that is removed before mapping.

[9] An advantage of the TWINS mission over previous ENA imaging missions is the nearly continuous magnetospheric coverage provided by the two spacecraft. With thousands of hours of ENA flux data, ENA fluxes can be sorted by solar wind and magnetospheric conditions. The data intervals used in this study, which occurred during January and February 2009, were selected based on a requirement for quiet magnetospheric conditions (Dst index > −30 nT) with solar wind speeds of 400 km/s < V_{SW} < 600 km/s. The combination of these requirements with that of the satellite being at least 4 R_E above the xy-plane yielded 138.7 hours of data. Data were obtained from both satellites (47% from TWINS-1).

[10] The LOS-integrated, density-weighted phase space density, $j_{ENA}/\sigma E$, energy spectra for spatial bins in three different regions of the magnetosphere are shown in Figure 3. These plots include the fits used to determine the ion temperature assigned to each bin. These spectra and fits represent a) the inner magnetosphere with the bin containing (x, y) = (−5,−2), b) the near-Earth magnetotail: (−12,5), and c) the distant magnetotail: (−27,9). The error bars shown are based on the error in the flux assigned to a particular energy within each pixel in instrument coordinates and the number of times the particular energy and spatial bin in the plane is populated. The ion temperatures determined from the psd spectrum in each spatial bin of the GSM xy-plane for the selected intervals are shown in Figure 4a. Spatial bins that do not contain monotonically decreasing average flux values

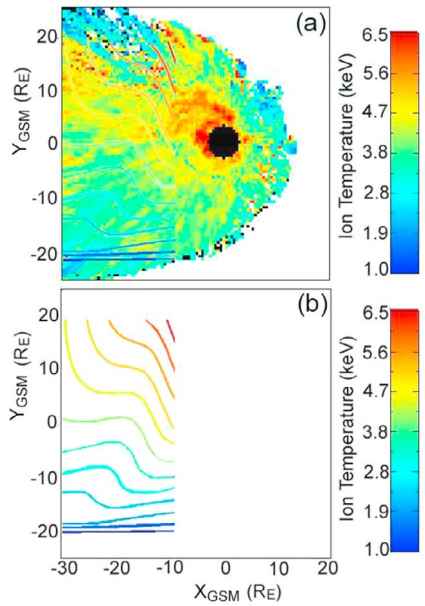

Figure 4. (a) Ion temperature image mapped onto the xy-plane in GSM coordinates with the Sun to the right. A black disc with radius 3 R_E, centered at the Earth, indicates the region where our analysis is not applicable. (b) Contours of constant ion temperature, with the same color bar as the ENA-based ion temperature measurements, as predicted by the finite tail width model of *Spence and Kivelson* [1993]. The spatial extent of the model predictions is limited to the region of overlap between model and observations. The same contours are also overlaid on the image in Figure 4a.

in at least 4 of 6 energy bins or do not meet goodness-of-fit requirements are assigned no-temperature color values (white and black, respectively).

3. Discussion

[11] There is a noticeable dawn-dusk temperature asymmetry in the magnetotail in Figure 4a. At roughly 20 R_E downtail, the ion temperature increases from approximately 2.5 keV on the dawnside to approximately 5 keV on the duskside. This asymmetry is consistent with *in situ* Geotail measurements reported by *Wang et al.* [2006] and *Guild et al.* [2008]. The region of cold temperatures at the top of Figure 4a is consistent with a cold flank observed by *Terasawa et al.* [1997]. The ion temperatures also agree in magnitude with those modeled for fast solar wind conditions by *Tsyganenko and Mukai* [2003]. We note that detection of an ion temperature gradient in this region of the magnetosphere with *in situ* spacecraft measurements required an accumulation of 3.5 [*Wang et al.*, 2006] and 6 [*Guild et al.*, 2008] years of data, respectively, while the ENA-derived measurements are an accumulation of less than 6 days of data spread over two months of mission time. These observations highlight the importance of a global view of the magnetosphere, as provided by the TWINS ENA instruments, and the substantial data rates resulting from having dual instruments.

[12] The dawn-dusk ion temperature asymmetry in the quiet-time magnetosphere is consistent with the predictions of a finite width magnetotail model developed by *Spence and Kivelson* [1993]. The underlying premise of the model is that as hot particles convect earthward under the influence of $E \times B$ motion, they also gradient and curvature drift across the tail in time stationary fields. A key prediction of the model is a strong dawn to dusk ion temperature asymmetry in the quiet-time magnetosphere. Shown in Figure 4b, with the same color bar as Figure 4a, are the predictions of the model for the magnetospheric regions that overlap with these ENA-derived ion temperatures (adapted from *Spence and Kivelson* [1993, Figure 5]). The model predictions are also overlaid on the ion temperature image of Figure 4a. There is good agreement in absolute ion temperature values and in the spatial distribution of the ion temperatures. Thus, these observations support the conclusion that duskward gradient/curvature drift and earthward $E \times B$ drift of ions lead to formation of a cross-tail pressure gradient from dawn to dusk. While previous studies confirmed the existence of an average ion temperature gradient, these new measurements obtained over a relatively short time demonstrate that the ion temperature gradient is an inherent feature of the quiet time magnetosphere even during times of transient moderately fast solar wind and that it exhibits significant spatial structure.

[13] We have presented a global view of ion temperatures in the magnetosphere during quiet conditions. When interpreting these measurements, several limitations of the technique must be considered. Ion distributions that are not thermal are rejected from the study and the optically thick region close to the Earth must be excluded. Also, the mapping algorithm assumes that the hottest point along the line of sight, and therefore the measured temperature, occurs in the equatorial plane, perhaps over-simplifying the complex and varying structure of the magnetosphere, especially in the magnetotail. However, we note that the analysis method used here to extract ion temperatures from the ENA observations is the only method currently available to provide continuous, global coverage of ion temperatures, especially in the magnetotail. Conventional inversions of ENA data using models of the ring current and geocorona are limited to the inner magnetosphere (2–7 R_E), data from the geosynchronous MPA instruments have been unavailable since 2008, and data from other *in situ* instruments require extended times to accumulate global maps. These ion temperature measurements can be used to place local measurements, such as those from THEMIS, in a global context and can be used to establish accurate boundary conditions for magnetospheric simulations.

[14] **Acknowledgments.** This work was carried out as a part of the TWINS NASA Explorer mission; work at WVU was supported under subcontract to the Southwest Research Institute.

References

Bame, S. J., D. J. McComas, M. F. Thomsen, B. L. Barraclough, R. C. Elphic, J. P. Glore, J. T. Gosling, J. C. Chavez, E. P. Evans, and F. J. Wymer (1993), Magnetospheric plasma analyzer for spacecraft with constrained resources, *Rev. Sci. Instrum.*, *64*, 1026–1033, doi:10.1063/1.1144173.

Denton, M., and M. G. G. T. Taylor (2008), Solar wind dependence of ion parameters in the Earth's magnetospheric region calculated from CLUSTER observations, *Ann. Geophys.*, *26*, 387–394, doi:10.5194/angeo-26-387-2008.

Fok, M.-C., R. A. Wolf, R. W. Spiro, and T. E. Moore (2001), Comprehensive computational model of Earth's ring current, *J. Geophys. Res.*, *106*, 8417–8424, doi:10.1029/2000JA000235.

Fok, M.-C., N. Buzulukova, S.-H. Chen, P. W. Valek, J. Goldstein, and D. J. McComas (2010), Simulation and TWINS observations of the 22 July 2009 storm, *J. Geophys. Res.*, *115*, A12231, doi:10.1029/2010JA015443.

Frank, L. A., K. L. Ackerson, W. R. Paterson, J. A. Lee, M. R. English, and G. L. Pickett (1994), The comprehensive plasma instrumentation (CPI) for the Geotail spacecraft, *J. Geomag. Geoelectr.*, *46*, 23–37.

Guild, T. B., H. E. Spence, E. L. Kepko, V. Merkin, J. G. Lyon, M. Wiltberger, and C. C. Goodrich (2008), Geotail and LFM comparisons of plasma sheet climatology: 1. Average values, *J. Geophys. Res.*, *113*, A04216, doi:10.1029/2007JA012611.

Hutchinson, I. H. (1987), *Principles of Plasma Diagnostics*, pp. 284–302, Cambridge Univ. Press, Cambridge, U. K.

Keesee, A., E. Scime, and M. Moldwin (2008), Remote measurements of ion temperatures in the terrestrial magnetotail, *J. Geophys. Res.*, *113*, A00A03, doi:10.1029/2008JA013130.

McComas, D. J., P. Valek, J. L. Burch, C. J. Pollock, R. M. Skoug, and M. F. Thomsen (2002), Filling and emptying of the plasma sheet: Remote observations with 1–70 keV energetic neutral atoms, *Geophys. Res. Lett.*, *29*(22), 2079, doi:10.1029/2002GL016153.

McComas, D. J., et al. (2009), The Two Wide-angle Imaging Neutral-atom Spectrometers (TWINS) NASA Mission-of-Opportunity, *Space Sci. Rev.*, *142*, 157–231, doi:10.1007/s11214-008-9467-4.

Scime, E. E., C. Pollock, M. Jahn, J. Kline, and A. Keesee (2002), Ion heating in the terrestrial magnetosphere during substorms and storm-time: MENA observations, *Geophys. Res. Lett.*, *29*(10), 1438, doi:10.1029/2001GL013994.

Shue, J.-H., J. Chao, H. Fu, C. Russell, P. Song, K. Khurana, and H. Singer (1997), A new functional form to study the solar wind control of the magnetopause size and shape, *J. Geophys. Res.*, *102*, 9497–9511, doi:10.1029/97JA00196.

Spence, H., and M. Kivelson (1993), Contributions of the low-latitude boundary layer to the finite width magnetotail convection model, *J. Geophys. Res.*, *98*, 15,487–15,496, doi:10.1029/93JA01531.

Terasawa, T., et al. (1997), Solar wind control of density and temperature in the near-Earth plasma sheet: WIND/GEOTAIL collaboration, *Geophys. Res. Lett.*, *24*, 935–938, doi:10.1029/96GL04018.

Tsyganenko, N. A., and T. Mukai (2003), Tail plasma sheet models derived from Geotail particle data, *J. Geophys. Res.*, *108*(A3), 1136, doi:10.1029/2002JA009707.

Wang, C.-P., L. R. Lyons, J. M. Weygand, T. Nagai, and R. W. McEntire (2006), Equatorial distributions of the plasma sheet ions, their electric and magnetic drifts, and magnetic fields under different interplanetary magnetic field Bz conditions, *J. Geophys. Res.*, *111*, A04215, doi:10.1029/2005JA011545.

Wing, S., and P. T. Newell (2002), 2D plasma sheet ion density and temperature profiles for northward and southward IMF, *Geophys. Res. Lett.*, *29*(9), 1307, doi:10.1029/2001GL013950.

Zaniewski, A., X. Sun, A. Gripper, E. Scime, C. Pollock, M. Jahn, and M. Thomsen (2006), Evolution of remotely measured inner magnetospheric ion temperatures during a geomagnetic storm, *J. Geophys. Res.*, *111*, A10221, doi:10.1029/2006JA011769.

Zhang, X. X., J. D. Perez, T. Chen, C. Wang, P. C. Brandt, D. G. Mitchell, and Y. L. Wang (2005), Proton temperatures in the ring current from ENA images and in situ measurements, *Geophys. Res. Lett.*, *32*, L16101, doi:10.1029/2005GL023481.

N. Buzulukova and M.-C. Fok, NASA Goddard Space Flight Center, Greenbelt, MD 20771, USA. (natalia.y.buzulukova@nasa.gov; mei-ching.h.fok@nasa.gov)

J. Goldstein and D. J. McComas, Southwest Research Institute, San Antonio, TX 78238, USA. (jerry.goldstein@swri.edu; dmccomas@swri.edu)

A. M. Keesee, E. Scime, and K. Tallaksen, West Virginia University, Morgantown, WV 26506, USA. (amy.keesee@mail.wvu.edu; escime@wvu.edu; ktallaks@mix.wvu.edu)

H. Spence, Institute for the Study of Earth, Oceans, and Space, University of New Hampshire, 8 College Rd., Durham, NH 03824-3525, USA. (harlan.spence@unh.edu)